



ELSEVIER

Combustion and Flame 133 (2003) 359–370

**Combustion
and Flame**

Premixed flame response to acoustic waves in a porous-walled chamber with surface mass injection

Wen-Wei Chu^a, Vigor Yang^a, Joseph Majdalani^{b,*}

^aPennsylvania State University, University Park, PA 16802, USA

^bMarquette University, Milwaukee, WI 53233, USA

Received 27 March 2002; received in revised form 15 January 2003; accepted 17 January 2003

Abstract

In order to study the internal coupling between flame dynamics and vortico-acoustic waves formed during solid propellant combustion, a numerical simulation of an idealized rocket combustion chamber is carried out. The chamber is modeled as a rectangular enclosure along whose porous walls a laminar mixture of premixed reactants is uniformly injected. The mathematical model is based on the conservation equations in two space dimensions. Full account is taken of variable thermo-physical properties and finite-rate chemical kinetics. Boundary conditions are specified using the method of characteristics that accommodates the transport of entropy, vorticity, and acoustic waves. The governing equations and associated boundary conditions are solved numerically using a preconditioning technique and a dual time-stepping integration procedure. For illustrative purposes, a propane-air mixture is injected through the chamber walls in an effort to emulate the flame evolution inside a solid-propellant rocket motor under laminar conditions. First, detailed flame structures under steady-state conditions are realized. Subsequently, traveling acoustic waves are imposed at the head end. Simulation results indicate that the oscillatory velocity exhibits a multidimensional structure caused by unsteady vorticity, pressure, and flame oscillations. Accordingly, the effects of laminar premixed flame oscillations are limited to a thin region above the burning surface. This region becomes thinner as the frequency of oscillations is increased. The flowfield outside the flame zone bears a striking resemblance to recent analytical solutions obtained in a geometrically similar chamber. © 2003 The Combustion Institute. All rights reserved.

Keywords: Numerical simulation; Flame dynamics; Injection driven chambers; Theroacoustic coupling

1. Introduction

In this article, the premixed laminar flame response to vortico-acoustic oscillations is investigated inside a porous-walled chamber simulating a solid rocket motor. Following the injection of a premixed flow of reactants across the chamber walls, the resulting thin laminar flame that forms in the vicinity of the porous wall is used to mimic the burning zone in

solid propellant rocket motors. Harmonic pressure fluctuations are superimposed to represent acoustic oscillations in actual motors. This work focuses on the thermo-acoustic boundary layer above the injection surface. This layer plays an important role in determining the energy exchange between unsteady combustion processes and core flow dynamics [1,2]. Understanding the mechanisms behind these thermo-acoustic energy exchange processes helps to improve our ability to predict combustion instabilities in rocket motors, gas turbines, and other large combustors.

Combustion instabilities arise in a number of

* Corresponding author. Tel.: 414-288-6877; fax: 414-288-7082.

E-mail address: maji@mu.edu (J. Majdalani).

Nomenclature

a	speed of sound, $\sqrt{\gamma RT}$
A	pressure amplitude
C_p	specific heat
\mathbf{E}, \mathbf{F}	convective flux vectors
$\mathbf{E}_v, \mathbf{F}_v$	diffusive flux vectors
e	specific total energy
k	thermal conductivity
M_i	molecular weight of species i
p	pressure
\dot{Q}	rate of heat release
\dot{q}	rate of heat release per unit mass
R	the ideal gas constant for reactants
T	temperature
t	physical time
u, v	velocities in x and y directions, respectively
V	specific volume
v_b	blowing velocity in a cold-flow model
v_f	transverse velocity directly above the flame
v_w	transverse velocity directly above the wall
x, y	Cartesian coordinates
Y_i	mass fraction of species i
λ	spatial wavelength of unsteady velocity
γ	ratio of specific heats
μ	dynamic viscosity
ν	kinematic viscosity
τ_c	characteristic time associated with heat release fluctuations
$\dot{\omega}_i$	mass production rate of species i
Ω	vorticity
Superscripts	
'	acoustic fluctuation
-	steady state
^	amplitude of fluctuating quantity
Subscripts	
a	acoustic mode
b	blowing condition for a cold flow
f	flame condition
i	chemical species i
s	entropy mode
v	vorticity mode
w	wall condition

physical contexts that generally exhibit a self-sustained coupling between unsteady chemical heat sources and chamber acoustics. Understanding their attributes is of crucial importance in the development of combustion devices such as solid rocket motors [3], liquid rocket engines [4], gas turbines [5], and pulsed combustors of the Helmholtz [6] and Rijke types [7].

Initially, random small-amplitude acoustic disturbances arise from the intrinsic flow instabilities in the chamber. If these disturbances oscillate in favorable phase with the rate of heat addition, they are amplified according to Rayleigh's criterion. In certain applications, the growing instability may reach a level sufficient to cause undesirable structural vibrations or outright failure of the system. A thorough understanding of this energy transfer mechanism requires detailed studies of a) *fluid dynamic processes* that dictate the environment in which chemical reactions occur, and b) *chemical processes* that provide the energy for driving thermo-acoustic instabilities. Clearly, the interaction between these two processes plays a key role in determining the dynamic behavior of unsteady motions in combustion chambers.

The present paper deals with the unsteady response of a laminar flame to traveling acoustic waves in a 2-D chamber. A simple geometry is selected in order to facilitate theoretical and numerical comparisons. Unlike other studies that have focused on turbulent flames in similar physical settings [8–12], the scope here will be limited to laminar flames only. The exploration of laminar flames will be shown to facilitate the identification of key mechanisms that can be corroborated by theoretical solutions.

The study begins in Section 2 by a description of the model and its attendant boundary conditions. The numerical scheme is briefly visited in Section 3 where it is followed by a steady-state solution of the problem at hand. After describing the mean flow and thermal characteristics in Section 4, the onset of unsteady disturbances is examined in Section 5. Therein, the thermo-acoustic coupling due to heat release is explored at different frequencies and spatial locations along the length of the chamber. The Rayleigh number is also invoked to explain the connection between vortico-acoustic waves and thermal oscillations. Finally, conclusions are provided in Section 6.

2. Formulation

2.1. Model

The planar domain is shown schematically in Fig. 1a. The chamber is closed at the head-end, while the

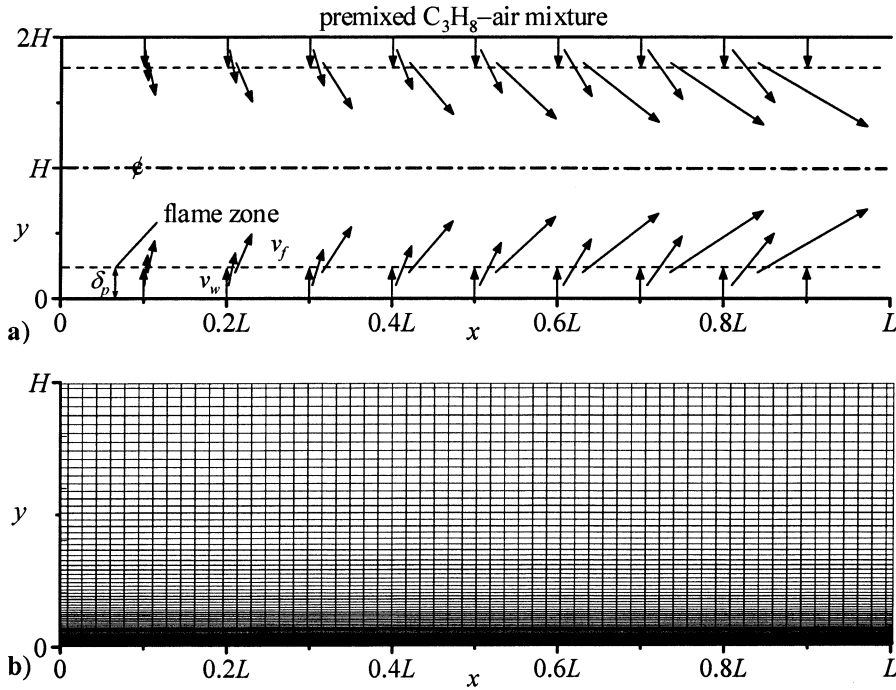


Fig. 1. Schematic diagram of the physical model illustrating a) the adopted space coordinates, flame zone location, and mean velocity evolution across the flame zone; and b) the nonuniform grid extending from the wall to the centerline.

porous top and bottom surfaces admit a premixed combustible mixture. The injection process simulates the gas-phase combustion and flow development in a rocket motor loaded with a homogeneous solid propellant. A similar configuration was experimentally studied by Sankar *et al.* [13]. Here we shall study the mutual coupling between flow oscillations and flame dynamics, with emphasis placed on the interactions among the acoustic, vortical, and entropy waves that arise in the chamber. But first, a numerical analysis based on the complete conservation equations and finite-rate chemical kinetics will be developed. In the process, various fundamental mechanisms, including vorticity generation and transport, flame oscillations, and acoustic motions, will be investigated.

2.2. Equations

The formulation is based on the conservation equations of mass, momentum, energy, and species concentrations for a multicomponent, chemically reacting system. Full account is taken of finite-rate chemical kinetics and variations in thermodynamical and transport properties. To start, the governing equations in 2-D Cartesian coordinates are written in the generic vector form

$$\frac{\partial \mathbf{Q}}{\partial t} + \frac{\partial}{\partial x}(\mathbf{E} - \mathbf{E}_v) + \frac{\partial}{\partial y}(\mathbf{F} - \mathbf{F}_v) = \mathbf{S} \quad (1)$$

where x and y represent the axial and transverse coordinates, respectively. Using standard descriptors, the vector of conserved variables \mathbf{Q} is defined by

$$\mathbf{Q} = [\rho, \rho u, \rho v, \rho e, \rho Y_i]^T \quad (2)$$

The inviscid flux vectors (\mathbf{E} , \mathbf{F}) and the viscous flux vectors (\mathbf{E}_v , \mathbf{F}_v) follow the definitions given in [14]. The thermal and mass diffusion processes are approximated by Fourier's and Fick's laws, respectively. The source term \mathbf{S} includes contributions from chemical reactions taking place inside the combustion chamber.

Within the temperature and pressure ranges of the present study, the specific heat, viscosity, and thermal conductivity are taken to be functions of temperature and can be approximated by fourth-order polynomials [15]. The mixture specific heat is obtained by mass-fraction weighing of each constituent species. Thermal conductivity and viscosity are calculated using Wilke's mixing rule. The binary mass diffusivity D_{ij} between species i and j is obtained using the Chapman-Enskog theory based on the Lennard-Jones intermolecular potential-energy functions [16]. The effective mass diffusion coefficient for species i in a

multicomponent mixture is related to the binary diffusion coefficients through Wilke's formula [17].

Because the present study is concerned with the effect of unsteady heat release and flow motion on chamber aeroacoustics, an accurate estimate of the flame speed and heat release rate is essential. The single-step global reaction mechanism proposed by Westbrook and Dryer [18] for hydrocarbon/air systems is therefore adopted because of its reasonable prediction of these two parameters. The small number of species involved further renders this model an attractive choice from the standpoint of computational efficiency.

2.3. Boundary Conditions

The method of characteristics is used to handle the boundary conditions. Because the flow is subsonic throughout the chamber, three physical conditions are specified at the inflow boundary and only one at the exit. The mass flow rate and temperature of the premixed gases are fixed at the porous walls, along with the no-slip condition that enforces normal injection of the reactants. At the head end, the axial velocity and pressure gradient, as well as the radial velocity gradient, are set to zero for steady-state calculations. This prevents the occurrence of numerically generated recirculation near the head end. It also coincides with the head-end boundary conditions used in mathematical idealizations of nonreactive core-flows [19]. For unsteady flow simulations, a periodic sinusoidal pressure oscillation is imposed at a known frequency. The axial velocity and temperature fluctuations are accordingly specified from the isentropic relations to generate a traveling acoustic wave propagating in the axial direction. Finally, flow symmetry is assumed along the centerline.

The exit boundary conditions are also treated carefully to avoid numerically generated, spurious reflecting waves. To this end, the methodology described by Watson and Meyer [20] is used to specify the flow properties at the exit section. The governing equations are rearranged into four decoupled relations controlling the vorticity, entropy, and acoustic wave propagation. The complete form of these relations can be obtained from [14]. The boundary conditions are imposed implicitly to be consistent with the treatment of the interior points.

3. Numerical method

The solution algorithm is based on a preconditioning technique developed to circumvent the computational difficulties arising in low Mach number reacting flows [21,22]. Temporal discretization is obtained

using a second-order dual-time stepping integration, and a second-order flux differencing technique for spatial discretization. The governing equations are treated in a fully coupled manner by means of an alternating-direction-implicit (ADI) factorization scheme [23]. The implicit treatment and dual-time stepping procedure guarantees a converged solution at every physical time step. This procedure also helps in capturing the transients in the flowfield and its attendant chemical reactions.

The numerical scheme described above is implemented to study the flame response to traveling acoustic waves in a porous chamber. The chamber has an effective aspect ratio of 20, being 1 m in length (L) and 0.05 m in wall-to-centerline height (H). A propane-air mixture having an equivalence ratio of 0.7 is injected across the porous walls at a flow rate of $0.21 \text{ kg m}^{-2}\text{s}^{-1}$, a temperature (T_w) of 350 K, and a pressure (p) of 1 bar. The flow rate translates into an injection velocity (v_w) of 0.206 m/s and a surface Mach number (M_w) of 5.6×10^{-4} where the speed of sound (a_w) is 368 m/s. After crossing the reactive flame zone ($y = \delta_p$), the gas velocity (v_p) increases to a speed of 1.154 m/s, at a Mach number (M_p) of 1.36×10^{-3} (see Fig. 1a). The computational grid is illustrated in Fig. 1b and consists of 60×100 non-uniform cells in the axial and transverse directions, respectively. In order to better resolve the rapid variations of flow properties in the flame zone, cells are clustered more closely near the porous boundary. The smallest cell is nearly 0.015 mm thick just above the transpiring wall.

4. Steady-state results

Before addressing the characteristics of the unsteady flow, it is helpful to examine the simulation results for the mean flowfield. Figure 2 illustrates the distributions of mean flow Mach number, vorticity, and gauge pressure under steady-state conditions. Because the configuration is symmetric, only the lower half of the chamber is displayed.

4.1. Mean velocity and pressure distributions

As indicated in Fig. 2, the coordinates $y/H = 0$ and 1 correspond to the porous wall and centerline, respectively. Throughout, the Mach number contours are shown to exhibit the 2-D structure typical of an injection-driven flow. For example, the Mach number increases linearly along the centerline from zero at the head end to 0.044 at the exit. The linear increase is consistent with cold-flow predictions for a similar chamber simulating a slab rocket motor [24]. Accord-

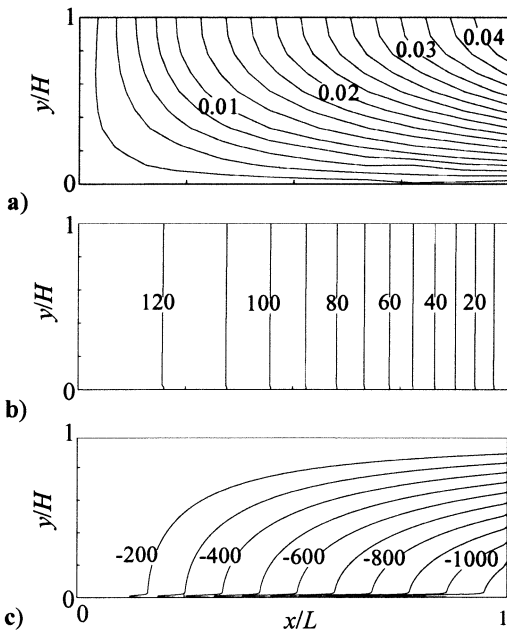


Fig. 2. Contours of a) Mach number, b) gauge pressure, and c) vorticity under steady-state conditions.

ing to cold-flow analysis, the mean velocity could be calculated from

$$u(x, y) = v_b \sqrt{F^2 + (x/H)^2 F'^2} \tag{3}$$

where v_b is the blowing or ejection velocity of the gases into the chamber. The large injection mean flow function is given by [24]

$$F = \cos \theta + (\pi/4)\varepsilon\{(\phi \cos \phi - \sin \phi)\ln|\tan(\phi/2)| + \cos \phi[A\phi - I(\phi)]\} + O(\varepsilon^2); \tag{4}$$

$$I(x) = x + 2 \sum_{k=1}^{\infty} \pi^{-2k}(1 - 2^{1-2k}) \frac{x^{2k+1}}{2k+1} \sum_{j=1}^{\infty} j^{-2k} \\ = x + \frac{1}{18}x^3 + \frac{7}{1800}x^5 + \dots \tag{5}$$

and the derivative is given by $F' = \frac{1}{2}\pi \sin \theta + O(\varepsilon)$. The asymptotic truncation order in Eq. 4 is gauged to the reciprocal of the injection Reynolds number, $\varepsilon = R^{-1} = v/(v_b H) = O(10^{-3})$. The trigonometric arguments $\theta = \frac{1}{2}\pi y/H$ and $\phi = \frac{1}{2}\pi - \theta$ are used for brevity. Based on this laminar mean flow solution, the Mach number can be determined from

$$M(x, y) = M_b \sqrt{\cos^2 \theta + \frac{1}{4}x^2 \pi^2 \sin^2 \theta} + O(\varepsilon M_b) \tag{6}$$

which, at the centerline, becomes $M(x, H) = \frac{1}{2}\pi(x/$

$H)M_b + O(\varepsilon M_b)$. Assuming that the bulk flow motion outside the flame zone can be approximated by the flow behavior of a nonreacting mixture (i.e., the propane-air gas products), one may set $v_b = v_f$ in the cold-flow equations. Thus, based on Eq. 6, the local Mach number can be expected to vary linearly along the centerline from zero to $\frac{1}{2}\pi(1/0.05)1.36 \times 10^{-3} = 0.043$ at the aft end. This result is clearly consistent with the downstream value displayed in Fig. 2a (although not shown on the graph, the numerical simulation predicts a maximum value of 0.044). Had the injection speed enhancement due to chemical reactions been ignored, the Mach number prediction at the downstream end would have been significantly underestimated (in this case, to 0.018). We thus conclude that, despite the adequacy of cold-flow models in approximating the gas motion outside the flame zone, the thermally adjusted speed v_f should be used to represent the equivalent blowing speed rather than the wall injection speed v_w . Otherwise, the usefulness of a cold-flow model can be severely compromised. The increase in effective gas injection can be attributed to the presence of chemical reactions and accompanying volumetric dilatations that are not present in the equivalent cold-flow model.

In like fashion, the pressure contours in Fig. 2b display an almost one-dimensional distribution that is weakly sensitive to the downstream location. No discernible variation in the transverse direction is observed, except for the small change arising from the volume dilation in the near-wall flame zone. These observations may be attributed to the low injection Mach number and can be corroborated by the theoretical results obtained without chemical reactions. In fact, based on [24], the mean-pressure varies according to

$$P(x, y) = P - \frac{1}{2}\rho v_b^2 \left[\frac{1}{4}\pi^2(x/H)^2(1 + \frac{1}{2}\pi\varepsilon \sin \theta) + \cos^2 \theta \right] \tag{7}$$

Along the centerline, it is clear that the transverse variation is manifested by the $\cos^2 \theta$ term, which is too small to be considered. On the other hand, the diminution in gauge pressure along the chamber length can be calculated to be $\frac{1}{8}\pi^2 \rho v_b^2 (x/H)^2$. Unlike the cold-flow simulation where all thermodynamic properties are kept constant, the density in the actual simulation varies along the chamber axis. At $x = L$, a density of 0.182 kg m^{-3} can be used to predict a pressure drop of nearly 120 Pa. This value concurs with the actual pressure decrease recorded in the actual simulation and shown in Fig. 2b (the maximum recorded pressure was 125 Pa).

4.2. Mean flow vorticity

To understand the sources of mean flow vorticity, attention can be turned to the Crocco-Vazsonyi equation. Subsequently, the material derivative of vorticity is expanded into

$$\begin{aligned} \frac{D\Omega}{Dt} = & (\Omega \cdot \nabla)\mathbf{u} - \Omega(\nabla \cdot \mathbf{u}) - \nabla V \times \nabla p + \nu \nabla^2 \Omega \\ & - \mu \nabla V \times (\nabla \times \Omega) + \frac{4}{3} \mu \nabla V \times \nabla(\nabla \cdot \mathbf{u}) \end{aligned} \quad (8)$$

where $\Omega = \nabla \times \mathbf{u}$ and $V = 1/\rho$ is the specific volume. In the present 2-D simulation, the vortex stretching mechanism $(\Omega \cdot \nabla)\mathbf{u}$ disappears. Vorticity is generated at the wall because of the no-slip condition that forces the parallel component of velocity to vanish along the porous surface [19]. Vorticity varies rapidly in the flame zone where both the volume dilation $\Omega(\nabla \cdot \mathbf{u})$ and baroclinicity $\nabla V \times \nabla p$ become important. Their influence is evidenced in Fig. 2c by the sudden emergence of vorticity overshoot near the surface.

The last two terms in Eq. 8 represent viscous damping and both appear to be secondary because of the large injection Reynolds number and the small mean flow velocity gradients in the entire chamber. In the absence of viscous dissipation, baroclinicity, and volumetric dilation outside the flame zone, the mean flow vorticity shown in Fig. 2c appears to be nearly conserved during its downstream convection. Its magnitude increases almost linearly from zero at the head end to 1152 s^{-1} at the aft end. To a good approximation, it can be evaluated from [24] via

$$\begin{aligned} \Omega = & -\frac{1}{4} \pi^2 (x/H^2) v_b \cos \theta + O(\varepsilon) \approx 1000 v_b \\ = & 1154 \text{ s}^{-1} \end{aligned} \quad (9)$$

This value concurs with the mean vorticity at the aft end. Here too, the use of a non-reactive formulation for the bulk vorticity outside the flame zone seems appropriate.

4.3. Mean temperature and heat generation

To complete our coverage of flowfield attributes, the mean temperature distributions are presented in Fig. 3 at various axial locations ranging from $x/H = 2$ to 17. The proximity to the head end is purposefully targeted to ensure laminar conditions. Due to the uniformly distributed heat of reaction along the surface, the overlaid temperature curves appear to be independent of the axial location. A one-dimensional

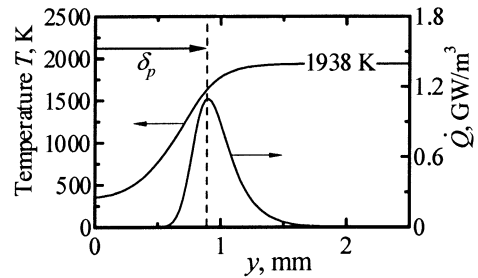


Fig. 3. Mean temperature and heat release above the porous surface of several axial stations corresponding to $x/H = 2, \dots, 7, \dots, 12, \dots, 17$. Due to the short distance from the head-end wall, laminar premixed flame conditions prevail over this axial range.

variation in the y direction is observed. The weak thermal sensitivity to the axial position can be attributed to the geometric aspect ratio and larger gradients in the transverse direction. Apparently, the downstream flow convection exerts hardly any influence on the flame structure. As shown in the graph, the temperature increases from the wall injection value of 350 K to a maximum of 1938 K just past the flame edge, at $y = \delta_p = 2 \text{ mm}$. The thickness δ_p is used to denote the premixed flame standoff distance, which is approximately 0.9 mm. Due to the rapid inward convection, this maximum temperature spreads uniformly across the core. The climbing temperature segment shown in Fig. 3 is sustained by a non-zero heat input curve for \dot{Q} .

It may be useful to note that the calculated flame temperature of 1938 K agrees with the chemical equilibrium result of 1915 K predicted by the NASA CET93 code [15]. The slight discrepancy may be due to the more detailed reactions incorporated in the CET93 calculations. The injection velocity of 20.6 cm/s agrees well with the experimental value of 20.9 cm/s measured by Metghalchi and Keck [25]. This agreement further supports the current methodology based on global chemical kinetics.

The typical S-shaped temperature curve displayed in Fig. 3 can be ascribed to the expected thermal surge across the flame zone. The retention of an almost-constant core temperature may be caused by the strong convective action that brings the hot products closer to the centerline. As demonstrated by Majdalani and Van Moorhem [24], the transverse penetration of injectants can be significant, especially in planar configurations, where the lack of curvature enables the injected mixture to draw nearer to the core before merging into the axial mainstream.

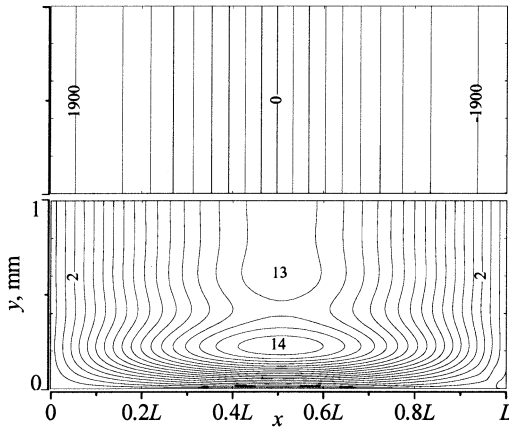


Fig. 4. Contour plots of instantaneous acoustic pressure and axial velocity fluctuations at 400 Hz.

5. Unsteady flow results

After steady-state solutions are reached, periodic flow oscillations are imposed at the head end in an effort to excite acoustic waves at prescribed frequencies. The boundary conditions along the burning surface are left unchanged with respect to those used during steady-state simulations. Following other experimental and numerical benchmark studies [8–10], the impressed oscillation frequency is varied from 100 to 800 Hz, while the amplitude of pressure fluctuations (A) is set at two percent of the mean pressure (≈ 160 dB). According to acoustic theory [26], the natural frequencies of the simulated chamber can be estimated from

$$f_m = ma_f / (2L); \quad a_f = \sqrt{\gamma RT_f} = 845 \text{ m/s} \quad (10)$$

where $\gamma = 1.265$, $R = 292 \text{ J kg}^{-1}\text{K}^{-1}$, and $T_f = 1938 \text{ K}$. Note that, due to the small thickness of the flame zone, the vast portion of the chamber cavity is filled with product gases such as CO_2 , H_2O , and air. For this reason, physical properties to be used in Eq. 10 are derived from the C_3H_8 -air products whose molecular weight averages $28.47 \text{ kg kmol}^{-1}$. Hence, for a unit chamber length, the problem's natural frequencies can be estimated from $f_m = 423m$, for $m = 1, 2, \dots$, etc.

5.1. Unsteady pressure and velocity fluctuations

Figure 4 illustrates the instantaneous isobaric contours of the fluctuating pressure and iso-velocity fields for $f = 400 \text{ Hz}$. This value is only 5.4% smaller than the first fundamental frequency of the combustion chamber at $m = 1$. Here the fluctuating variables are obtained by subtracting mean values, calculated

over a complete cycle of oscillation, from their total time-dependent quantities. As a result of this sifting operation, a well-defined traveling wave motion is realized. The wave motion bears a striking resemblance to the standing mode shape described in [27]. Therein, the physical setting is identical except that a nonreacting gas is used. The analytical predictions obtained in [27] under laminar conditions seem to agree quite favorably with the current results.

With respect to the unsteady pressure and velocity, Fig. 4 suggests the same overall mode shape by exhibiting a pressure node and a velocity antinode midway along the chamber length at $x = 0.5L$. The near-wall combustion interactions do not seem to exert any marked influence on the general character of the acoustic velocity, so long as the flow remains dominated by longitudinal strain rates.

It should be noted that the current contours are quite similar to those described in [27], which were based on the closed-form expression

$$u'(x, y, t) = \frac{A}{a_f \rho} \left[\sin\left(m\pi \frac{x}{L}\right) \sin\left(m\pi a_f \frac{t}{L}\right) \right] \quad (11)$$

$$- F \sin\left(m\pi \frac{x}{L} F\right) e^{\xi} \sin\left(m\pi a_f \frac{t}{L} + \Phi\right) \quad (11)$$

where $A = 2000 \text{ Pa}$, $a_f = 846 \text{ ms}^{-1}$, $m = 2$, $\omega = 2\pi f_m$, and

$$\zeta = -\zeta \int_0^{y/H} F^{-3}(x) dx = -\frac{1}{\pi} \xi \left\{ \ln \tan \left[\frac{1}{2} \left(\theta + \frac{\pi}{2} \right) \right] + \sec \theta \tan \theta \right\}, \quad \xi = \nu \omega^2 H \nu_f^{-3} \quad (12)$$

$$\Phi = -\text{Sr} \int_0^{y/H} F^{-1}(x) dx = -\frac{2}{\pi} \text{Sr} \ln \tan \left[\frac{1}{2} \left(\theta + \frac{\pi}{2} \right) \right], \quad \text{Sr} = \omega H / \nu_f \quad (13)$$

In the above, Sr represents the Strouhal number based on the oscillation frequency and thermally enhanced injection velocity ν_f . Viscous damping is materialized in the form of ξ which accounts for the relative magnitude of viscosity. This viscous parameter controls the exponential decay function ξ which, in turn, dictates, in part, the penetration depth of the unsteady, vortico-acoustic wave [28]. Note that, in Eq. 11, the second term represents the vortical wave whose amplitude diminishes as the distance from the porous walls is increased. Theoretically, the unsteady motion near the midsection plane is solely prescribed by the inviscid, pressure-driven fluctuations which

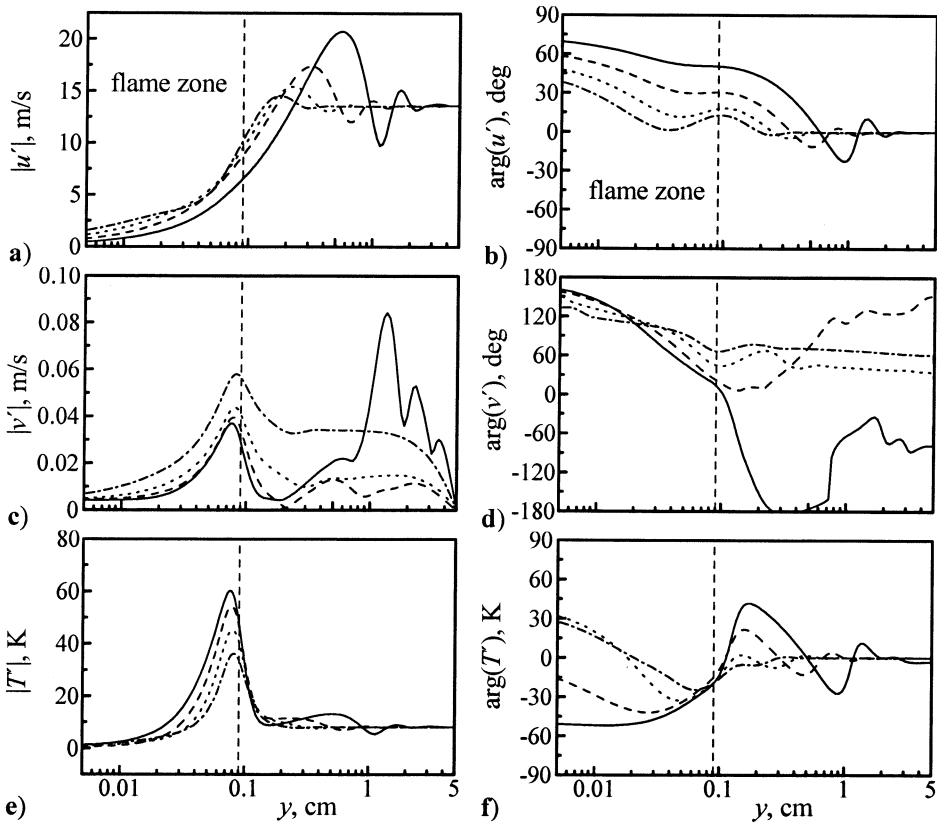


Fig. 5. Amplitudes and phases of unsteady velocity and temperature fluctuations at $x/H = 3$ and four frequencies corresponding to $f =$ — 100 Hz, - - - 200 Hz, ··· 400 Hz, ····· 800 Hz.

persist after both vortical and thermal fluctuations have vanished. Equations 11–13 were derived for the axial component of velocity in the context of a non-reacting gas oscillating inside a porous channel with sidewall injection. In order to partially account for the effect of near-wall combustion, the injection velocity here is based on v_f in lieu of the actual blowing velocity at the wall.

As seen in Fig. 4, rotational effects are lifted off the burning surface by approximately 10% due to the presence of flame interactions. In addition to the expected coupling effects between acoustic and vorticity waves near the surface, the velocity fluctuations seem to exhibit an additional 2-D correction resulting from interactions between the vortico-acoustic wave and the nonuniform temperature distribution across the flame zone. Away from the surface, vortical and thermal effects quickly decay and are dominated by a simple inviscid wave structure. This is manifested in Fig. 4 by a one-dimensional acoustic velocity distribution over the range $0.4 \leq y/H \leq 1$. The unsteady wave amplitude of approximately 13 ms^{-1} can be interpreted in light of the established theory of

aeroacoustics [19]; accordingly, an acoustic velocity amplitude of $A/(a_f \rho) \approx 13 \text{ ms}^{-1}$ can be expected near the core. However, due to the thermal suppression of vorticity waves across the flame zone, a relatively small overshoot in unsteady velocity is observed near the wall. This overshoot is caused by the pairing of vorticity and acoustic waves and is much smaller than the typical 100% overshoot value reported in cold-flow simulations. The attenuation of the vorticity wave is due, in part, to the strong volume dilation across the flame zone.

The formation of acoustically induced shear layers is examined in Fig. 5 by plotting the transverse distributions of both amplitudes and phases of the fluctuations u' , v' , and T' at different frequencies. The flame location is also included to facilitate the discussion. The most salient features are the shortening in spatial wavelength (λ) and the reduction in wave amplitude with frequency. These observations are in agreement with former studies of nonreacting flows [24,27–30]. For example, following the technique described in [24], the diminution in wavelength may be inferred from Eq. 11 to be $\lambda = v_f F/f_m$. This

relation clearly displays an inverse relation between λ and f_m . The reduction in total wave amplitude with frequency is probably due to the reduced wavelength which, in turn, causes the coupling between acoustical and vortical waves to take place nearer to the flame zone. There the phase interference with thermal waves leads to a faster attenuation of vortical strength. Outside the flame zone, the vortical presence is further exacerbated by the increased shearing, reversal, and damping of fluid particles over shorter length and time scales.

The observed behavior may once more be illuminated by the Crocco-Vazsonyi equation. Using similar arguments to those given in Section 4 to explain the mean flow vortical growth, the interplay between volume dilation and baroclinicity in the flame zone can be used to explain the attenuation of unsteady vortical growth. In addition, the wavelength of the vortical motion is increased in the flame zone due to the increasing wave propagation speed (partly triggered by volumetric dilation). At the outset, the combination of volume dilation, baroclinicity, and increased wave propagation speed in the flame zone tend to reduce the role of vorticity near the wall, especially as compared to the case of a nonreacting flow. This explains why the largest unsteady amplitudes occur outside the flame zone and later decay as the core is approached. In particular, note that, despite the presence of chemical reactions, the amplitude of v' is smaller than that of u' by the order of the Mach number, $M_f = O(10^{-3})$. This result is significant insofar as it confirms the theoretical predictions obtained from cold-flow studies of the core flow [27].

5.2. Velocity decomposition

In order to better understand the coupling between the flame response and velocity waves, it is helpful to identify the separate contributions of pressure-driven, boundary-driven, and entropy-driven disturbances. Following [31], the Chu-Kovácsznay mode decomposition approach is implemented to subdivide the total velocity fluctuation into three parts representing acoustical, vortical, and thermal oscillation modes. This approach has been previously employed by Flandro [19] and Majdalani [27], who have separated the velocity field into two parts: an irrotational, acoustical u'_a , and a rotational, vortical u'_v . Since the current study involves chemical reactions, the contribution from heat fluctuations is added in the form of a thermal, entropy-driven correction u'_s . The total fluctuation can hence be split into

$$u' = u'_a + u'_v + u'_s \tag{14}$$

On the one hand, the acoustic velocity u'_a is directly correlated with the pressure fluctuation through the

acoustic impedance, $\bar{\rho}\bar{a}$. This product varies rapidly in the flame zone and is proportional to the inverse of \sqrt{T} . On the other hand, the rotational part u'_v incorporates the effects of unsteady vorticity generation and transport. The newly introduced velocity fluctuation u'_s results from the unsteady heat release originating in the flame zone. Based on acoustic theory [26], this quantity can be approximated by

$$u'_s \approx \frac{k}{\bar{\rho}C_p\bar{T}} \frac{\partial T'_s}{\partial x} \tag{15}$$

where T'_s represents the non-isentropic temperature fluctuation. Since the temperature gradient only exists in the transverse direction, the effect of entropy waves on the axial velocity fluctuation can be ignored. Its influence on the transverse velocity fluctuation must be retained, however, so long as it is capable of exciting large transverse oscillations [14].

5.3. Unsteady temperature fluctuations

Figure 5c illustrates the effect of frequency on the amplitude and phase of temperature fluctuations. The corresponding steady-state distributions of temperature and heat release rate have already been examined in Fig. 3. Pursuant to the velocity decomposition, the temperature fluctuation can be obtained by superimposing the acoustic and entropy-driven contributions. The acoustic component T'_a obeys the isentropic relation governing the acoustic pressure. In the current study, it has an amplitude of 8 K in the core region. The non-isentropic component T'_s is approximately proportional to the product of entropy fluctuation and mean temperature [26]. In view of Eq. 15, it can be expressed by

$$T'_s \approx \dot{q}'\tau_c/C_p \tag{16}$$

where \dot{q}' is the fluctuation in the rate of chemical heat release, and τ_c represents its associated characteristic time. As shown in Fig. 5c, the fluctuating temperature response exhibits a peak directly below the line of maximum mean temperature. This peak reaches about 60 K at a frequency of 100 Hz and then drops to nearly 35 K at 800 Hz. The thermal oscillations also persist longer and therefore, penetrate deeper into the chamber core at lower oscillation frequencies. This result can be attributed to the intimate coupling near the wall with the longitudinal vortico-acoustic waves whose role is to sustain these thermal oscillations. Since the vortico-acoustic depth of penetration diminishes at higher frequencies, so will the depth of thermal fluctuations. This effect is observed in both modulus and phase variations in Fig. 5c.

So long as the vortico-acoustic waves cause the flame to flutter in the vicinity of the wall, thermal

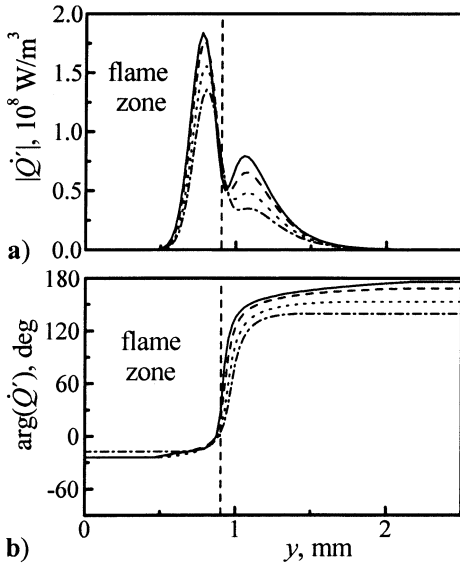


Fig. 6. Amplitudes and phases of unsteady chemical heat release rate at $x/H = 3$ and four frequencies corresponding to $f =$ — 100 Hz, - - - 200 Hz, ··· 400 Hz, · - · - · 800 Hz.

fluctuations can be sustained. These fluctuations are empowered by alternating high-temperature sweeps into the preheat zone that can periodically expedite the ongoing chemical combustion and attendant heat of reaction. The behavior of thermal fluctuations near the wall can be adequately represented by the Arrhenius relation connecting reaction rates and temperatures. When sufficiently removed from the flame zone (where heat is constantly supplied), the unsteady temperature becomes dominated by the high-capacity, pressure-driven ‘mass-like’ response T'_a that always prevails in the core region [31]. Between the flame edge and the core, the entropy fluctuation T'_s is smoothed out due to heat conduction and the thermal flywheel effect that accompanies the traveling acoustic wave.

Because the flame oscillation is induced by the vortico-acoustic motion, the characteristic time τ_c described in Eq. 16 may be estimated by the period of acoustic oscillations, $\tau_c \approx 1/f_m = 2L/(ma_p)$. A low-frequency acoustic motion will lead to a larger-amplitude temperature fluctuation while allowing a deeper penetration of the vortical wave into the chamber core. These theoretical predictions are clearly reflected in the current numerical results.

5.4. Response to unsteady heat addition

The unsteady heat release rate is shown in both amplitude and phase in Fig. 6 at one axial position and four different frequencies. For the reasons given to explain the behavior of the temperature fluctuations,

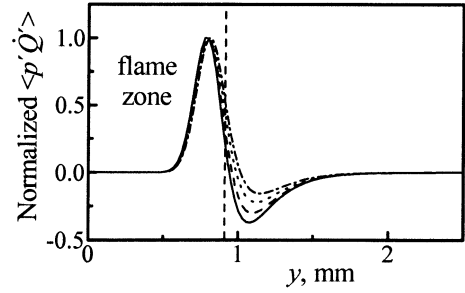


Fig. 7. Normalized Rayleigh parameter at $x/H = 3$ and four frequencies corresponding to $f =$ — 100 Hz, - - - 200 Hz, ··· 400 Hz, · - · - · 800 Hz.

the amplitude and depth of penetration of the heat waves decay more rapidly at higher frequencies. However, two uneven peaks in \dot{Q} are observed below and above the flame location. The value of the peak outside the flame zone is approximately 60% of the inner one, which is consistent with the experimental observation of Sankar et al. [13]. From a theoretical perspective, the two energy peaks serve as a combination of an acoustic monopole and a dipole source for driving the observed oscillations [26]. In order to explain the observed damping outside the flame zone, attention can be turned to the fundamental role of heat addition in driving or suppressing the unsteady fluctuations.

In principle, the amplification of an acoustic wave p' due to periodic heat input supplied at a rate \dot{q}' can be characterized using Rayleigh's parameter [32]:

$$\langle p' \dot{q}' \rangle = \int_{\tau_c} p'(\mathbf{x}, t) \dot{q}'(\mathbf{x}, t) dt \quad (17)$$

An impressed acoustic excitation will grow when the above parameter is positive. Thus, if heat is added at the moment when the combustion mixture is locally expanding (i.e., during a favorable pressure phase), the dilatational thermal energy is positively gained insofar as it leads to a more pronounced volumetric expansion. When this occurs, the thermal wave can be considered to be in favorable phase with the acoustic motion that it tends to sustain and amplify. Conversely, if heat is added at the moment of local gas compression (i.e., during an adverse pressure phase), the effect of thermal addition is that of opposing the volumetric contraction. Wave cancellation takes place as some of the acoustic energy is eliminated.

In the problem at hand, two regions of positive and negative Rayleigh numbers can be recognized. As shown in Fig. 7, the two regions of favorable and adverse thermo-acoustic coupling are delineated by the flame standoff distance. These regions are identified by plotting the Rayleigh parameter $\langle p' \dot{q}' \rangle$ at

$x/H = 3$ and the same four frequencies. In both regions, the magnitude of $\langle p'q' \rangle$ diminishes at higher modes, indicating a weaker thermo-acoustic coupling at higher frequencies. The weaker coupling at higher frequencies may explain the diminution in temperature oscillations at higher f_m in Fig. 5c. In particular, the negative Rayleigh number for $y > \delta_p$ is indicative of a damped out region in which the role of unsteady heat addition switches to that of vortico-acoustical wave attenuation. This feature may explain the damping character of unsteady energy release in the outer flame region ($y > 0.9$ mm).

6. Conclusions

This study has focused on the interactions between acoustic waves and premixed flame dynamics in porous chambers. In the process, the complete conservation equations were numerically solved while accommodating variations in thermo-physical properties. Finite-rate chemical kinetics were also enabled to spatially resolve the flame structure. Both mean and unsteady flame attributes were examined in various oscillatory flow environments. The unsteady motions were found to comprise contributions from acoustical, vortical, and thermal modes that strongly depend on the frequency of the impressed acoustic wave. The thermal oscillations were found to be restricted to a thin region near the wall. Outside this flame zone, the spatial distribution of pressure and velocity were found to closely resemble the theoretical predictions obtained from cold-flow solutions based on the flame-enhanced gas injection speed. In particular, the flow was found to be mainly isothermal and the fluctuating velocity in the transverse direction appeared to be smaller than the axial component by the order of the Mach number M_f . Furthermore, the amplitude of all fluctuating components decreased at higher frequencies. This behavior applied to the acoustic boundary layer thickness as well. To explain the pairing between thermo-acoustic and vortico-acoustic waves, an energy cascade among these three separate fluctuation modes was identified. Within the flame standoff distance, the thermo-acoustic response was found to be favorable to vortico-acoustic growth. Outside this region, however, a negative Rayleigh number was confirmed, signaling an adverse thermo-acoustic coupling. As a result of the thermal oscillations induced by the vortico-acoustic wave, the rate of unsteady heat release was found to exhibit two uneven peaks. These could be attributed to the Arrhenius type of temperature dependence on reaction rates. The two peaks could also be viewed as a combination of an acoustic monopole and a dipole source for driving flow oscillations. The amplification and suppression roles of thermo-acoustic cou-

pling due to unsteady heat addition were both conclusively realized by calculating local Rayleigh numbers. By focusing on the laminar flame behavior, this study has permitted the identification of several important mechanisms and features characterizing both mean and unsteady variables affecting combustion instabilities. Key features of the mean flow under reactive conditions include the small size of the flame zone due to premixing and the rapid velocity increase of the transverse velocity across the flame zone. As usual, premixing appears to be an adequate assumption for simulating the pyrolysis of solid propellant grains in which fuel and oxidizer particles are embedded within the same matrix. The identification of a thermally enhanced velocity directly above the flame zone is another key result that has enabled us to analyze the same problem using cold-flow formulations. Due to rapid combustion and termination of chemical reactions in close proximity to the walls, it is realized that the vast majority of the chamber remains isothermal; hence, a non-reactive approach could be uniformly applied by relocating the chamber walls to the edge of the flame zone while, at the same time, using the thermally enhanced blowing speed along the newly displaced chamber boundaries. This study also identifies thermally induced baroclinicity and dilatational gradients to be responsible for inducing a slight distortion in mean flow vorticity near the walls. In relation to unsteady motions, this work helps unravel the effects of thermal fluctuations on the chamber's vortico-acoustic waves. Due to the difference in phase oscillations between thermal and vortical waves, the Richardson overshoot mechanism observed in cold-flow studies is weakened under reactive conditions [28]. By comparison with inert flow studies of oscillatory waves in porous channels and tubes, the unsteady velocity overshoot near the wall is much smaller here. The vortical wave attenuation can be attributed to the strong volume dilation across the flame zone and to the wave cancellation that accompanies thermal waves with dissimilar phases. The overall wave attenuation is further increased at higher frequencies that tend to promote a faster shear reversal and wave decay over shorter spatial length scales. The accelerated decay in amplitude and penetration depth of temperature fluctuations can also be attributed to the weakening in thermo-acoustic coupling at higher frequencies. This weakening is commensurate with the reduced Rayleigh number that is observed at higher oscillation modes. This study also suggests the presence of two regions within the flame zone in which favorable and adverse thermo-acoustic coupling are present, respectively. These two regions are delineated by the flame standoff distance beyond which the Rayleigh number turns negative, thus signaling the onset of thermo-acoustic damping.

References

- [1] S. Apte, V. Yang, *Combust. Flame* 131 (2002) 110–31.
- [2] T.-S. Roh, S.V. Apte, V. Yang, Twenty-Seventh Symposium (International) on Combustion, The Combustion Institute, Pittsburgh, 1998, pp. 2335–2341.
- [3] F.E.C. Culick, V. Yang, in *Nonsteady burning and combustion stability of solid propellants*, L. De Luca, E.W. Price, M. Summerfield, (Eds.), v. 143, AIAA Progress in Astronautics and Aeronautics, Reston, VA, 1992, p. 719–779.
- [4] F.E.C. Culick, V. Yang, in *Liquid rocket engine combustion instability*, V. Yang, W.E. Anderson, (Eds.), V. 169, AIAA Progress in Astronautics and Aeronautics, Reston, VA, 1995, p. 3–37.
- [5] T.C. Lieuwen, Y. Neumeier, B.T. Zinn, *J. Prop. Power* 15 (1999) 613–6.
- [6] Y.M. Tang, G. Waldherr, J.I. Jagoda, B.T. Zinn, *Combust. Flame* 100 (1995) 251–61.
- [7] B. Entezam, W.K. Van Moorhem, J. Majdalani, *J. Numer. Heat Trans. A* 41 (2002) 245–62.
- [8] S. Apte, V. Yang, *AIAA J.* 39 (2001) 1577–86.
- [9] S. Apte, V. Yang, *AIAA J.* 40 (2002) 244–53.
- [10] Apte, S., Yang, V., *Proceedings of the Combustion Institute*, vol. 28, The Combustion Institute, Pittsburgh, 2000, p. 903–910.
- [11] T.M. Liou, W.Y. Lien, P.W. Hwang, *J. Prop. Power* 14 (1998) 282–9.
- [12] T.-M. Liou, W.-Y. Lien, *J. Prop. Power* 11 (1995) 600–6.
- [13] S.V. Sankar, J.I. Jagoda, B.T. Zinn, *Combust. Flame* 80 (1990) 371–84.
- [14] Chu, W.-W., *Dynamic responses of combustion to acoustic waves in porous chambers with transpiration*, PhD Thesis, Department of Mechanical Engineering, Pennsylvania State University, College Park, 1999.
- [15] McBride, B.J., Gordon, S., *CET93 and CETPC: An Interim Updated Version of the NASA Lewis Computer Program for Calculating Complex Chemical Equilibria with Applications*, TM-4557, NASA, Technical Report, 1994.
- [16] R.C. Reid, J.M. Prausnitz, B.E. Poling, *The Properties of Gases and Liquids*. 4th ed., McGraw Hill, New York, 1987, p. 388–490.
- [17] C.R. Wilke, *Chem. Engng Prog.* 46 (1950) 95–104.
- [18] C.K. Westbrook, F.L. Dryer, *Combust. Sci. Technol.* 27 (1981) 31–43.
- [19] G.A. Flandro, *J. Prop. Power* 11 (1995) 607–25.
- [20] W.R. Watson, M.K. Myers, *AIAA J.* 29 (1991) 1383–89.
- [21] I.S. Tseng, V. Yang, *Combust. Flame* 96 (1994) 325–42.
- [22] S.Y. Hsieh, V. Yang, *Intl J. Comput. Fluid Dyn.* 8 (1997) 31–49.
- [23] R.M. Beam, R.G. Warming, *AIAA J.* 16 (1978) 393–401.
- [24] J. Majdalani, W.K. Van Moorhem, *Aerosp. Sci. Technol.* 5 (2001) 193–207.
- [25] M. Metghalchi, J.C. Keck, *Combust. Flame* 48 (1982) 191–210.
- [26] A. D. Pierce, *Acoustics, an introduction to its physical principles and applications*, Acoustical Society of America, New York, 1989.
- [27] J. Majdalani, *J. Appl. Math. Phys. (ZAMP)* 52 (2001) 33–61.
- [28] J. Majdalani, *AIAA J.* 37 (1999) 505–8.
- [29] J. Majdalani, T.-S. Roh, *Proc. Roy. Soc. A* 456 (2000) 1625–57.
- [30] J. Majdalani, W.K. Van Moorhem, *AIAA J.* 36 (1998) 241–8.
- [31] B.-T. Chu, L.S.G. Kovásznyai, *J. Fluid Mech.* 3 (1957) 494–514.
- [32] Rayleigh, J.W.S., *Theory of Sound*, Dover, New York, 1954.